2025-24-0096 Published 07 Sep 2025

Analysis and Simulation of Fuel Consumption and Emissions in a Heavy-Duty Diesel Truck under Real-World Driving Conditions for Hybridization and Waste Heat Recovery

Teresa Donateo and Talha Mujahid University of Salento

Pietropaolo Morrone and Angelo Algieri University of Calabria

Citation: Donateo, T., Mujahid, T., Morrone, P., and Algieri, A., "Analysis and Simulation of Fuel Consumption and Emissions in a Heavy-Duty Diesel Truck under Real-World Driving Conditions for Hybridization and Waste Heat Recovery," SAE Technical Paper 2025-24-0096, 2025, doi:10.4271/2025-24-0096.

Received: 11 Apr 2025 Revised: 29 Jun 2025 Accepted: 29 Jun 2025

Abstract

Heavy-duty vehicles contribute significantly to global greenhouse gas emissions and are now facing challenges in meeting emission regulatory standards, particularly cold-start operations. These challenges are particularly significant during transient operations, where fuel efficiency drops and emissions peak due to suboptimal thermal conditions. Advanced powertrains that use hybridization and waste heat recovery with phase-changing materials offer potential pathways to mitigate fuel consumption and emissions under real-world driving conditions. Still, they need to be accurately sized, and the energy flows handled to overcome the disadvantages of increased mass and complexity. This investigation lays the groundwork for the development of advanced power systems by implementing a scalable, map-based model for heavy-duty diesel engines. The model is validated using an open-access dataset related to a heavy-duty vehicle equipped with a 6-cylinder diesel engine, which performed 28 different trips on the same route with the same driver. The trips are executed with three different payload values and contain both cold-start and hot-start operating conditions. The validation is based on quasi-static modeling of the vehicle powertrain. The proposed model can accurately predict fuel consumption and CO2 emissions for all trips, with an average relative error of 2.4%. The results of the investigation also include preliminary sizing and analysis of a hybrid electric configuration that exploits the synergy between hybridization and waste heat recovery. In comparison to the original powertrain, the proposed powertrain resulted in a roughly 15% reduction in fuel consumption and a 37.5% increase in exhaust temperature. These findings demonstrate the potential for integrated hybrid and waste heat recovery systems to enhance fuel economy in heavy-duty transportation while supporting compliance with emission regulations.

Introduction

Regulatory frameworks such as the World Harmonized Heavy-Duty Certification (WHDC), Federal Test Procedure (FTP), and China VI Standards [1] have reshaped the design and performance evaluation of Heavy-Duty Vehicles (HDVs). These cycles aim to simulate a wide range of operating conditions, encompassing urban, rural, and highway driving scenarios, to ensure compliance across various loads and terrains [2, 3, 4]. These standardized test cycles primarily capture steady-state and idealized conditions, which often fail to reflect the dynamic and stochastic nature of on-road operations. Discrepancies between laboratory conditions and real-world performance remain a significant hurdle. Real Driving Emissions (RDE) tests [5], leveraging Portable Emissions Measurement Systems (PEMS) [6, 7], have revealed critical insights into the transient engine loads [8] and exhaust temperature profiles experienced by HDVs in actual use. PEMS-based studies have underscored the underperformance of emission control systems during cold starts [9, 10], where exhaust aftertreatment systems may not reach optimal operating temperatures, and during low-load driving [11, 12]. In response to these challenges, the Euro VII legislation introduces stricter emission limits and more robust testing protocols for HDVs [13], emphasizing real-world compliance and cold-start operations [14]. Set to replace Euro VI standards, Euro VII mandates tighter control of NO_x, particulate matter, and carbon emissions [15], alongside improved durability requirements for emission control systems over extended

lifespans. The regulation also reinforces the role of RDE tests, expanding measurement conditions to capture better real-world driving scenarios, including a broader range of ambient temperatures and altitudes [8]. By aligning regulatory requirements more closely with real-world operation, Euro VII aims to bridge the gap between certification cycles and on-road emissions, ensuring that HDVs remain compliant under diverse driving conditions [16]. These challenges are particularly significant during transient operations, where fuel efficiency drops and emissions peak due to suboptimal thermal conditions.

On-board diagnostics (OBD-II) systems are essential for monitoring, analyzing, and optimizing performance, fuel consumption, and emissions in heavy-duty vehicles (HDVs). Over the years, advancements in sensor technologies, wireless communication, and cloud-based analytics have transformed OBD-II from a basic diagnostic tool into a real-time, telematics-based monitoring platform [17, 18]. These systems are essential for ensuring compliance with stringent emissions regulations, optimizing fuel consumption, and enhancing predictive maintenance strategies [19]. The integration of the Global Positioning System (GPS), Controller Area Network (CAN) bus, and advanced telematics systems enables high-resolution data collection [20], allowing for the accurate evaluation of the performance of HDVs operating in diverse driving conditions. By integrating GPS data with OBD-II and CAN bus systems, researchers and fleet operators can correlate driving behavior with fuel efficiency, emissions trends, and route characteristics [21, 22]. The OBD-II protocols, which are widely used in modern HDVs, allow real-time monitoring of critical performance parameters, including engine speed (RPM) [23], fuel injection rate (mg/stroke) [24], exhaust gas temperature (EGT) [25], and throttle position parameters which serve as input to the map-based engine model developed in this study. These parameters enable precise engine performance assessment and are used in this investigation for the development of a map-based engine model [26]. GPS systems track parameters such as altitude, speed, acceleration, and geographical coordinates, which help analyze energy demand variations across different road conditions [20]. This integration is particularly useful in evaluating driving cycles, as it enables precise identification of urban, suburban, and highway driving patterns [27].

The modeling of internal combustion engines (ICEs) in HDVs plays a crucial role in evaluating fuel consumption, emissions, and overall engine performance under various operating conditions, as well as in proposing advanced power systems. Engine modeling approaches provide predictive insights into torque, power, fuel efficiency, and emissions behavior without the need for extensive physical testing. Recent advancements have led to the development of a variety of modeling techniques, ranging from empirical map-based models to physics-based, semi-empirical, and machine learning-driven methodologies. Empirical map-based models [28] are widely used to estimate fuel consumption and CO_2 emissions based on engine speed and torque inputs, offering computational efficiency and ease of integration into vehicle simulations. On the other hand, physics-based approaches, such as reduced-order combustion models and organic Rankine cycle (ORC) simulations [29], are applied to real-time engine control and energy recovery strategies in HDVs. In parallel, machine learning techniques, particularly neural networks, random forests, and recurrent architectures such as long short-term memory (LSTM) and gated recurrent units (GRU), are gaining traction due to their high prediction accuracy for both fuel consumption and emission trends [30, 31]. These methods have shown strong performance in predicting NO_x and CH_4 emissions under transient conditions, where traditional models often struggle. Moreover, hybrid or gray-box models, which combine physical engine modeling with machine learning based learning, offer a powerful compromise between accuracy and computational speed, beneficial for hardware-in-the-loop (HIL) applications and real-time control systems [30]. Map-based engine modeling is still a widely used approach in automotive engineering, particularly for simulating ICEs in HDVs and for the design and analysis of hybrid electric configurations [32]. This method relies on empirical data to create maps that represent engine behavior under various operating conditions, facilitating accurate predictions of fuel consumption and CO_2 emissions [33] by relating the fuel flow rate $\dot{m}_{fuel}$ to engine operating conditions in terms of speed and torque:

$$\dot{m}_{fuel} = g\left(N, T_{engine}\right) \tag{1}$$

Here, g denotes the function derived from the fuel consumption map. This approach is particularly useful in vehicle simulation models designed to assess fuel efficiency under various driving scenarios. Map-based engine models offer several advantages, including computational efficiency and ease of implementation. They are well-suited for real-time applications and are commonly used in HIL simulations [34]. However, their reliance on empirical data means they may lack accuracy outside the tested operating conditions and may not capture transient behaviors effectively [35]; therefore, they are not suitable for predicting pollutant emissions.

Mean Value Engine Models (MVEMs) offer a balance between computational efficiency and accuracy by averaging engine variables over entire cycles, thus capturing the essential dynamics without delving into high-frequency cycle-to-cycle variations. They operate on the principle of averaging key engine parameters such as intake manifold pressure, exhaust manifold pressure, and engine speed over complete engine cycles [36]. This approach simplifies the complex interactions within the engine, making it feasible to model transient behaviors effectively. Finally, 1D and 3D CFD provide a high-fidelity representation of exhaust gas behavior by resolving spatial gradients in velocity, temperature, and species concentration [37] but are not suitable for the present investigation because they require detailed information on the geometry, configuration, and control of the engine.

The map-based approach also offers the advantage of scalability. A scalable procedure to obtain engine maps of a new engine from available data of another ICE with

the same technology was proposed by Rizzoni et al. [38] and validated by Sorrentino et al. [39] by scaling a diesel engine from 102.6 kW to 67.2 kW. The scalability is significant in the development of hybrid electric vehicles. Hybridization has emerged as a viable solution to mitigate environmental impacts while improving fuel efficiency and vehicle performance. By integrating ICEs with electric propulsion systems, hybrid HDVs can optimize energy consumption, reduce emissions, and enhance overall vehicle performance. The implementation of hybridization strategies in HDVs involves different powertrain configurations, each offering distinct advantages and trade-offs [40, 41]. Hybridization offers several benefits, including enhanced fuel efficiency, reduced emissions, and improved performance. By leveraging regenerative braking, hybrid systems recover kinetic energy during deceleration and store it in an energy storage system for later use, thereby reducing reliance on fuel-based propulsion. Research studies indicate that fuel savings of up to 30% can be achieved in urban driving conditions where frequent braking and acceleration occur [42]. Additionally, the reduction in fuel consumption directly translates into lower CO_2 and NO_x emissions, helping hybrids comply with stringent environmental regulations such as Euro VI and U.S. EPA greenhouse gas (GHG) standards. Furthermore, the electric motor enhances vehicle torque delivery and responsiveness, making hybrid powertrains particularly advantageous for heavy-duty applications that require high power output during acceleration and hill climbing. Series hybrid electric vehicles have the advantages over parallel configurations of decoupling engine speed from vehicle speed, but at the cost of reduced efficiency and increased powertrain mass [43].

In conventional internal combustion engines (ICEs), more than 60% of the primary fuel energy is lost [44] because of heat loss through the exhaust pipe, cooling energy to prevent the engine from sticking, residual heat from the coolant to increase the engine power and net efficiency, and the convection of residual heat on the engine's surface. In diesel engines, one of the most significant sources of thermal efficiency loss is the enthalpy of the exhaust gas. Real-world exhaust temperature data reveals significant variations across engine speeds and loads, emphasizing the importance of tailoring heat recovery systems to specific driving conditions. Selective Catalytic Reduction (SCR) and Diesel Particulate Filters (DPFs) require optimal exhaust temperatures for efficient operation, which can be challenging during low-load urban driving. However, the energy flows are strongly dependent on the engine working point. The temperature and flow rate of exhaust gases change continuously during a driving cycle, not only due to dynamic variations in engine load and speed, but also due to variable boundary conditions, such as engine temperature and ambient conditions (temperature, pressure, and humidity). Moreover, the enthalpy of the exhaust gases decreases along the discharge line as the flow passes through the exhaust manifold, turbocharger turbines, after-treatment systems (like SCR and soot trap), muffler, and is finally discharged at the tailpipe.

Waste heat recovery is one of the key technologies proposed in the IRIDESCENT project ("Biodiesel hybrid electric bus with waste heat recovery (WHR) and storage"), which received funds from the European Union – NextGenerationEU through the Italian Ministry of University and Research (MUR). The goal of this project is to reduce the environmental impact associated with cold start operations of HDVs. It achieves this by integrating on-board WHR with ORCs, hybridization, biodiesel fuel utilization, and the deployment of thermal energy storage (TES) systems. To achieve the project's goal, a map-based model is developed in this study for a 6-cylinder diesel engine and validated using an open-access dataset related to an HDV.

The synergy between WHR and hybridization in an HDV has not been addressed extensively in scientific literature. Villani et al. [43] proposed a series hybrid electric configuration, finding an improvement between 12% and 17.6% in fuel consumption over the two regulatory cycles used for the investigation. The analysis proposed in [43] is based on a 1D model of the engine, without validation using experimental data for exhaust flow rate and temperature. A further study of the same research group revealed that better results can be obtained with a parallel configuration [45]. The novelty of the present investigation, compared to prior research, lies in the detailed analysis of fuel consumption, exhaust temperature, and flow rate using experimental data acquired during real-world tests performed under hot and cold-start conditions, thereby specifically addressing the critical aspect of Euro VII emission standards. The experimental data were not acquired by the authors but extracted from an open-access dataset [46]. However, to the authors' knowledge, this is the first time that this specific dataset has been analyzed in detail. A map-based model is proposed and extensively validated to estimate not only fuel consumption but also temperature and mass flow rate of exhaust gases. The model is used to assess the potential of hybridization and WHR under real-world driving conditions. Within this scope, a parallel architecture with the engine working at constant power but variable speed is proposed to stabilize exhaust energy and enhance WHR with ORC. Another innovative aspect of the investigation is the sizing of the electric drive as a compromise between fuel consumption, battery mass, and average exhaust temperature.

The Dataset

The vehicle analyzed in the present research is the Class 6 truck Isuzu FTR850 ATM, which is equipped with a 6-cylinder Euro III turbocharged intercooled diesel engine [46]. The primary specifications of the vehicle and its powertrain are detailed in Table 1 [47]. No exhaust after-treatment device is installed on the vehicle. The choice of this dataset was performed following an analysis of the accessible open data on medium and heavy-duty diesel trucks, which were found to be quite limited

TABLE 1 Relevant specification of the vehicle.

Vehicle	Isuzu FTR 850
Gross Vehicle Mass (GVM)	15500 kg
Gross Combination Mass (GCM)	24000 kg
Vehicle mass during tests	10740 kg
Payload	{0 kg; 1500 kg; 3000 kg}
Engine model	Isuzu 6HK1
Emissions standard	Euro 3
Displacement	7.79 liters
Number of Cylinders	6
Power	210 kW @ 1900 rpm
Torque	1080 Nm @1500- 1800 rpm
Fuel consumption (H-series)	0.342 lb/HP-h (208 g/kWh)
Transmission and drive type	Hydraulic controlled
Number of gears forward	6
Gear Ratios (inclusive of final ratio)	{38.9; 24.0, 13.85, 9.0,5.88, 4.24}
Tires	11 R22.5- 16PR (radius 0.52m)

compared to the amount of data available for passenger cars and buses. Unfortunately, it was not possible to find a dataset containing similar data for a diesel truck compliant with more recent emissions regulations.

The dataset comprises twenty-eight trips, with the first eight conducted with the flatbed unloaded, the next ten with a 3000 kg payload, and the last ten with a 1500 kg payload. All trips were performed in South Africa on the same vehicle by the same driver and following a standard route, with coincident starting and ending points, located at the University of Pretoria's Hatfield campus (Pretoria, South Africa), with a total distance of 61.7 km. The vehicle was equipped by Joubert et al. [46] with a PEMS, which is connected to the OBD-II power while driving and integrated with a Garmin GPS module. The acquisition frequency was 1 Hz for trips from #1 to #8 and 5 Hz for the other trips. The relevant variables recorded in the dataset that were used in this investigation are summarized in Table 2, together with their source (GPS, OBD-II, or PEMS). More details can be found in [46]. Unfortunately, the PEMS used for the investigation recorded emissions only of CO_2, CO, and NO_x. However, this investigation does not focus on pollutant emissions, so the lack of information on particulate matter is not of great consequence.

TABLE 2 List of relevant information from the dataset [46].

Variable	Description	Unit	Source
z	Altitude	m	GPS
T_{amb}	Ambient temperature	°C	PEMS
V	Vehicle speed	km/h	OBD-II
T_{cool}	Coolant temperature	°C	OBD-II
$\dot{m}_{fuel}$	Instantaneous fuel flow	g/s	OBD-II
$\dot{m}_{exh}$	Exhaust mass flow rate	kg/h	PEMS
T_{exh}	Exhaust temperature	°C	PEMS
$\dot{m}_{CO_2}$	Instantaneous mass of CO_2	g/s	PEMS
$\dot{m}_{NO_x}$	Instantaneous mass of NO_x	g/s	PEMS
$\dot{m}_{CO}$	Instantaneous mass of CO	g/s	PEMS

FIGURE 1 Speed profile and elevation of a real-world trip (trip #4)

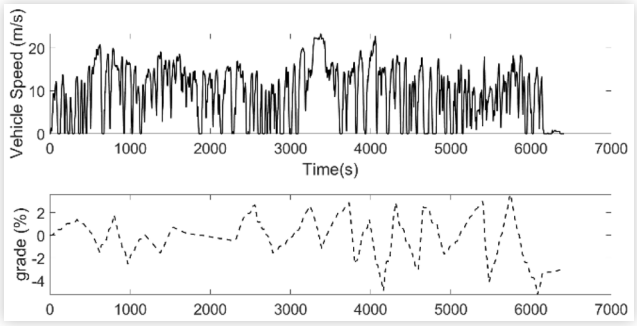

An example of a trip is shown in Figure 1, where the time histories of speed and grade are reported. About the grade profile, the altitude signal from GPS was corrected with geodetic information from Google Maps ©.

Real-World Driving vs Regulatory Driving Cycles

The first analysis performed on the dataset was a comparison with regulatory driving cycles used in scientific literature for the analysis of HDVs: WHVC, NYC Composite, NYB, HHDDT Cruise, FIGE, and Braunschweig. The speed-time profiles of these cycles are reported in the Appendix. The quantitative analysis of these cycles is based on key dynamicity parameters, providing valuable insights into vehicle dynamics (see Table 3).

In accordance with European regulations on emissions, the variability of driving cycles is measured by a parameter called Relative Positive Acceleration (RPA), defined as follows:

$$RPA_k = \frac{\sum_j h \cdot \left(v \cdot a_{pos}\right)_{j,k}}{\sum_j d_{i,j}} \tag{2}$$

Where $d_{i,j}$ is the distance related to the route section $k = \{u, r, m\}$ refers to the urban, rural, and motorway path; h is the time interval corresponding to the acquisition frequency; v is the vehicle speed. a_{pos} is the positive acceleration defined as;

$$a_{pos} = \frac{v_{i+1} - v_{i-1}}{2\Delta t} \tag{3}$$

For the dataset, the acceleration signal was obtained by differentiating the data of speed from the OBD and then filtering it.

The driving cycle of the dataset (Figure 1) combines the high dynamicity of cycles WHVC and Braunschweig, with the higher speeds of cycles HHDDT and FIGE. In fact, the speed trend of Figure 1 exhibits significant fluctuations

TABLE 3 Regulatory driving cycles vs trip #4.

	WHVC	NYC	NYB	HHDDT Cruise	FIGE	Braunschweig	Trip #4
Duration (s)	1800	1029	600	2083	1800	1740	6500
Distance (km)	10.6	4.0	0.9	37.1	29.4	10.9	62.6
Average Speed (km/h)	21.2	14.1	5.9	64.2	59.0	22.5	34.4
Max Speed (km/h)	66.2	57.9	49.6	95.4	91.1	58.2	84.0
Max Acc. (m/s^2)	1.6	2.1	3.1	0.9	3.9	2.4	2.5
RPA (m/s^2)	0.17	0.18	0.04	0.04	0.06	0.21	0.3

over time, indicating fast variations in driving patterns, grade, acceleration, and deceleration phases. Moreover, the selected trips are significantly longer, with an average driving time of 1.8 hours and an average distance of approximately 63 km.

The maximum acceleration and the RPA of the dataset cycle are quite unrealistic if no filter is applied. For this reason, a moving window average filter is used to accelerate the vehicle modeling process, ensuring it remains within the performance limits of the engine-gearbox system (see later in the paper).

Cold-Start vs Hot-Start

The available trips are classified in Figure 2 according to the vehicle mass and initial temperature of the cooling fluid. The cycles with an initial temperature higher than 79°C were considered "hot start". If the temperature was below 30°C, the trips were denoted as cold starts. Two mid-start trips were also identified (#1 and #11).

Figure 4 and Figure 5 try to correlate the overall fuel consumption and emissions to payload and initial coolant temperature.

Emissions of CO_2 are proportional, as expected, to fuel consumption, as shown in Figure 3. Note that the slope of the interpolating line in this figure (3.12 with R^2 = 0.9924) is coherent with the emission index reported in the scientific literature for diesel fuel [48]. Only for trip#19, there is a slightly discordant correlation between fuel consumption from OBD and CO_2 emissions from the PEMS. In this case, the measured CO_2 emissions are approximately 4% lower than expected based on the recorded fuel consumption.

By analyzing Figure 4, we can notice that fuel consumption increases with load while there is no apparent correlation with the initial coolant temperature. This is due to the limited fraction of trips that are traveled under cold-start operation. In fact, the average time for the coolant to reach 80°C is 400s for cold-start cycles. The time at which a cold-start trip reaches the threshold of 80°C is named Matching Coolant Temperature Time (MCTT).

In terms of NO_x emission (Figure 5), there is no clear correlation with payload and initial temperature, because

FIGURE 2 Classification of the trips according to initial temperature of the cooling fluid and vehicle mass.

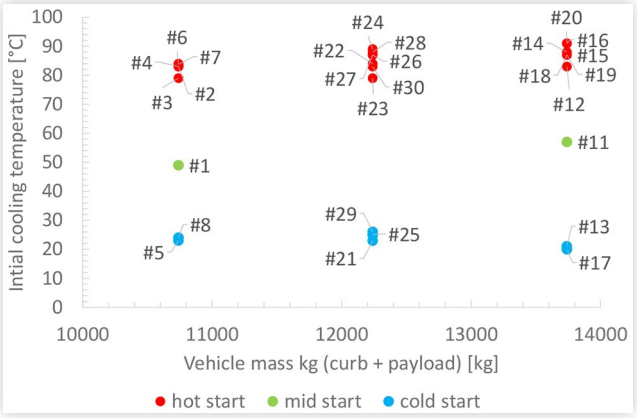

FIGURE 3 Correlation between fuel consumption and CO_2 emissions in the dataset.

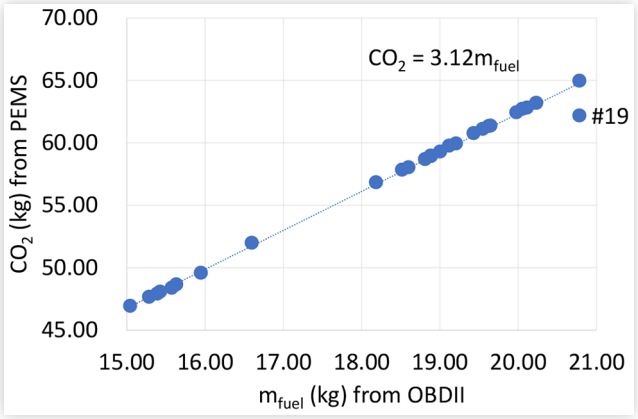

FIGURE 4 Effect of Payload and Initial Temperature on Fuel Consumption.

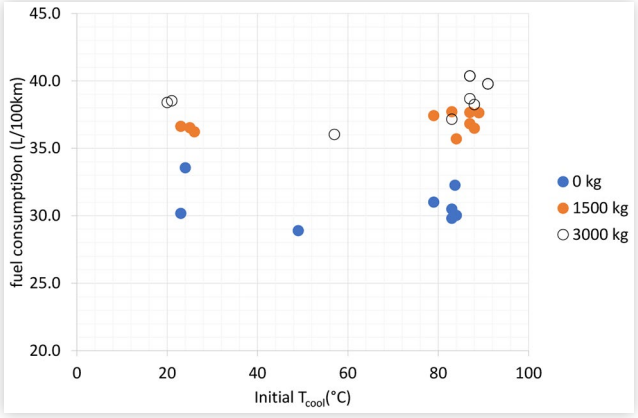

FIGURE 5 Effect of payload and initial coolant temperature on NO_X emissions.

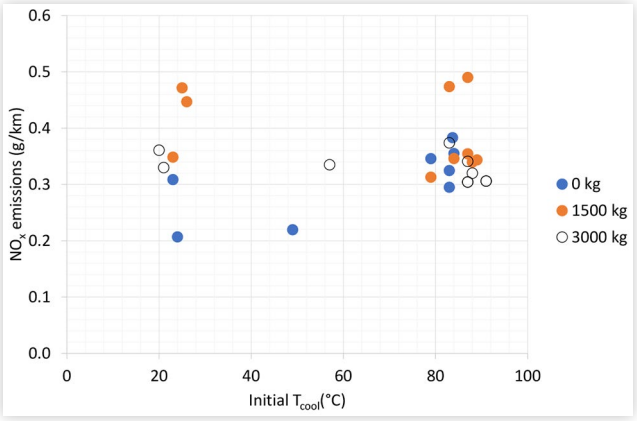

of the complex dynamic processes that determine the production of pollutant emissions. CO emissions are not shown because of the limited relevance for diesel engines. However, the results are as uncorrelated as in the case of NO_x values.

To put into evidence, the worsening of fuel consumption and pollutant emissions and the reduction of exhaust gases energy at cold-start operation, only the initial part of the trips was considered.

Despite being related to the same vehicle, route, and driver, the speed profiles of the trips can vary significantly, as shown in Figure 6, which displays the initial part of the driving cycles without payload. To ensure uniformity in the analysis, we removed the initial records before starting the vehicle and aligned all trips relative to a reference trip by shifting their indices accordingly. In this figure, cold-start trips, represented by dashed lines, generally exhibit a more gradual acceleration profile in the initial stages, likely due to engine warm-up effects and reduced efficiency during the early phases of operation. In contrast, hot start trips, depicted with solid lines, display a more immediate acceleration response, suggesting that a pre-warmed engine contributes to improved vehicle dynamics and quicker attainment of higher speeds.

The trends of coolant temperature for the no-payload trips are shown in Figure 7. An MCTT of 410s was

FIGURE 6 Speed Profiles of the eight trips without payload. Top: hot-start trips. Bottom: cold-start trips.

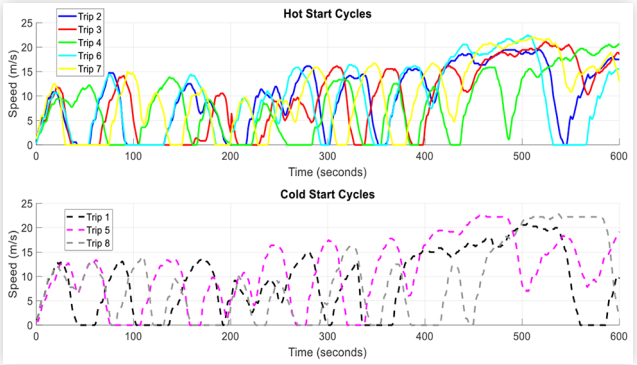

FIGURE 7 Coolant Temperature Profiles from Trips #1 to #8 (no payload).

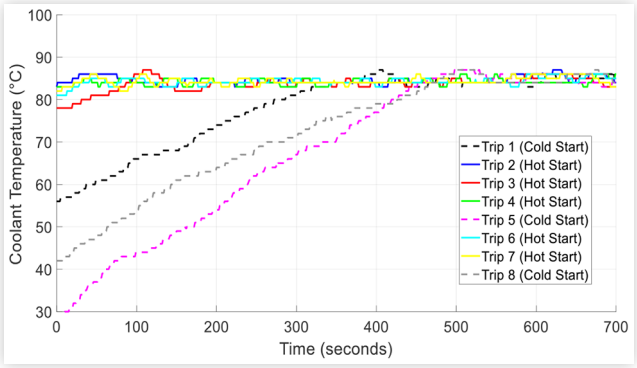

identified for this set of trips. The hot start trips display a more consistent temperature profile with periodic fluctuations, corresponding to variations in engine load and acceleration phases. Trip 6 shows more aggressive temperature spikes compared to Trip 4, suggesting different driving patterns or load conditions. The cold start trips, despite eventually converging towards the hot start temperature range, remain lower for a significant duration, reinforcing the inefficiencies and increased pollutant emissions associated with cold engine operations.

To quantify the effect of cold start, for each level of payload, three representative trips were selected, using the similarity in the speed profile as the criterion. The selected trips are #5 for cold start and #4 and #6 for hot start for the no-payload case.

The exhaust temperature profiles of the selected trips, shown in Figure 8, highlight the thermal behavior of the Isuzu truck under different starting conditions. The cold-start trip (Trip 5) exhibits a significantly lower initial exhaust temperature, starting below 50°C and gradually rising over time. This delayed temperature increase is indicative of the engine and exhaust system requiring time to reach optimal operating conditions. In contrast, the hot start trips (Trips 4 and 6) start with higher initial exhaust temperatures, exceeding 100°C, and show a more immediate stabilization at elevated levels. The observed trends confirm that cold-start operation reduces

FIGURE 8 Exhaust temperature profiles of the Isuzu truck for one cold start (Trip 5) and two hot start conditions (Trips 4 and 6).

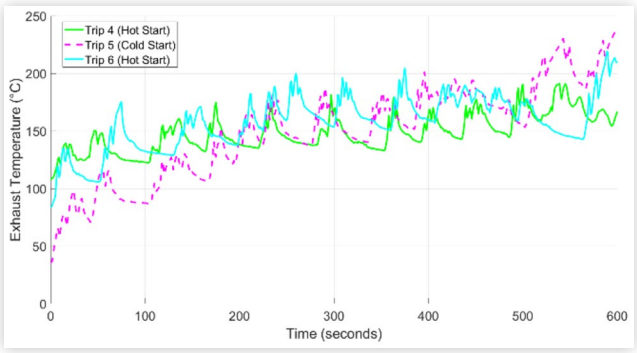

the time required for the engine (and, if available, the aftertreatment system) to reach optimal performance.

The cumulative profiles of fuel consumption and NO_x emissions are reported in Figures 9 and 10, respectively. The cold-start trip (Trip #5) consistently exhibits the highest cumulative fuel consumption values due to increased fuel injection requirements and inefficient combustion during the engine warm-up phase. Hot start trips show a more gradual increase, highlighting the benefits of operating a pre-warmed engine.

The cumulative NO_x emissions graph (Figure 10) shows that the cold start trip accumulates emissions at a higher rate than the hot start trips (Trips #4 and #6). This suggests that lower initial engine and exhaust temperatures contribute to an increase in NO_x formation.

The additional emissions and fuel consumption of trip#5 were estimated by calculating the difference, at MCTT, between the cumulative values for trip #5 and the average of the other two cycles. The procedure of trip selection, identification of MCTT, and computation of additional emissions and fuel consumption was repeated for the other two levels of payload, and the results are reported in Table 4. The differences in cumulative emissions and fuel flow at the matching coolant temperature time for selected trips show notable variations with the payload, while the MCTT is almost the same. There is no clear trend of additional emissions vs payload as already found when analyzing the whole trips (Figure 5).

FIGURE 9 Cumulative fuel consumption of the Isuzu truck for one cold start (Trip 5) and two hot start conditions (Trips 4 and 6).

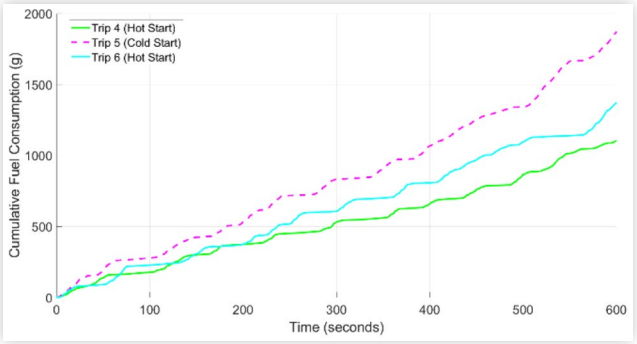

FIGURE 10 Cumulative NO_x emissions of the Isuzu truck for one cold start (Trip 5) and two hot start conditions (Trips 4 and 6).

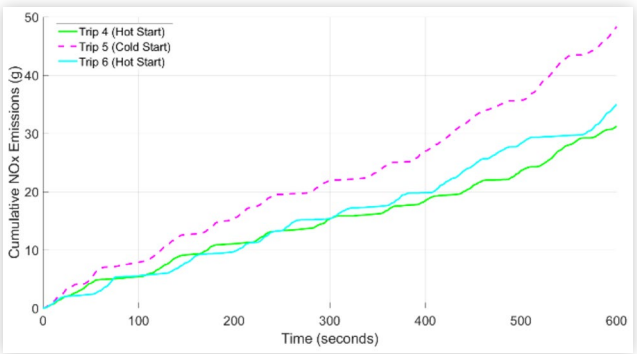

TABLE 4 Differences in Cumulative Emissions and Fuel Flow at the Matching Coolant Temperature Time.

Payload	MCTT (s)	Fuel (g)	CO_2 (g)	NO_x (g)
0 kg (trip 5 vs 4 and 6)	410	346.9	1088	8.3
1500 kg (trip 29 vs 22 and 27)	408	101.0	310.4	2.1
3000 kg (trip 17 vs 14 and 15)	379	199.7	625.6	4.7

Modeling Methodology

The goal of the modeling methodology was to replicate the vehicle's behavior under real-world driving emissions and develop a scalable model for use within the IRIDESCENT project framework to address hybridization and WHR.

A backward quasi-static simulation approach with a discretization of h = 1s was considered for the vehicle and its components. Starting from the time histories of speed, $V(i)$ and grade $\alpha(i)$ for a specific trip, the power request at the vehicle wheels is calculated as:

$$P_w(i) = \frac{1}{2} C_d \cdot A_f \cdot \rho_a \cdot V(i)^3 + M \cdot g \cdot C_r \cdot V(i) \cdot \cos\alpha(i) + M \cdot g \cdot \sin\alpha(i) \cdot V(i) + M_i \cdot a(i) \cdot V(i) \quad (4)$$

Where C_d and C_r are the drag and rolling friction coefficients, respectively. The rolling coefficient depends on vehicle speed and pneumatic pressure p_w, however, a constant value is often used in applying Eq. (4). M is the mass of the vehicle (inclusive of curb mass, driver, trailer, and payload), M_i is the mass inclusive of the inertial effects ($\cong 1.1M$ [43]), $\rho_a(t)$ is the ambient density, A_f is the frontal area of the vehicle estimated from a frontal view of the vehicle ($A_f = 4.7m^2$), a(i) is the acceleration.

In a conventional powertrain with only fuel as an energy source, the engine must provide, at any time, propulsive power and satisfy the request for power from the auxiliaries:

$$P_{ice}(i) = P_w(i) / \eta_{gb} + P_{aux}(i) \quad (5)$$

Where η_{gb} is the efficiency of the gearbox and P_{aux} the parasitic power of the auxiliary systems (lighting, radiator fan, cooling pump, etc.).

Choice and Validation of Vehicle Parameters

Literature data were used to select values of C_d and C_r for the reference vehicle, as shown in Table 5.

TABLE 5 Choice of vehicle parameters.

Parameter	References	Suggested	Selected
C_d	Hammache et al. [49], Arts et al. [50]	0.4-0.7	0.6
C_r	Arts et al. [50]	0.008	0.008
η_{gb}	Vehicle manual	0.96	0.96
P_{aux}	Arts et al. [50]	2-10kW	2 kW

To validate the selected values, available declared values of maximum speed and grade were used, but they refer to a version of the vehicle equipped with the ISUZU 6HK1-TCN [51]. This engine is characterized by a reduced displacement (6.7 L) and produces 176 kW @ 2400 rpm and 706 Nm between 1450 and 2400 rpm [51].

The maximum speed of the vehicle was determined by comparing the available full-load engine power at each of the six gears with the required power from Eq. (5) (Figure 11).

The traction forces $F_t(V,j)$ the engine generates at a certain speed and gear were calculated as:

$$F_t(V,j) = \eta_{gb}(j) \cdot T_{e,FL}(\omega_e) / R_w \quad (6)$$

Where $T_{e,FL}(\omega_e)$ is the full-load torque of the engine at speed $\omega_e = \gamma(j) \cdot \frac{V}{R_w}$, with $\gamma(j)$ overall gear ratio engine-to-wheel with gear j = 1, ..., 6 (reported in Table 1) and R_w is the wheels radius (0.52m).

Gradeability plots of Figure 12 were obtained by solving, for each gear j=1,..,6, the following equation obtained with the assumption cosα(t) ≅ 1 and constant speed:

$$\sin\alpha(V) = \frac{F_t(V,j) - \frac{1}{2} C_d A_f \rho_a V^2 - M \cdot g \cdot Cr}{M \cdot g} \quad (7)$$

Similarly, acceleration plots can be calculated assuming no grade α(t) ≅ 0:

$$a(V) = \frac{F_t(V,j) - \frac{1}{2} C_d A_f \rho_a V^2 - M \cdot g \cdot Cr}{M_i} \quad (8)$$

FIGURE 11 Graphical calculation of the max speed. Black line: required traction power, colored lines: full-load power of the engine with six gear ratios.

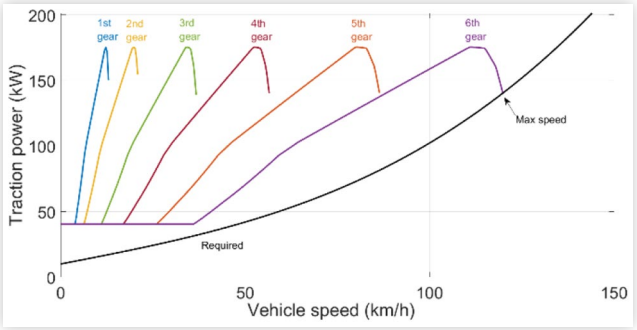

FIGURE 12 Gradeability curves for a vehicle mass of 10470kg.

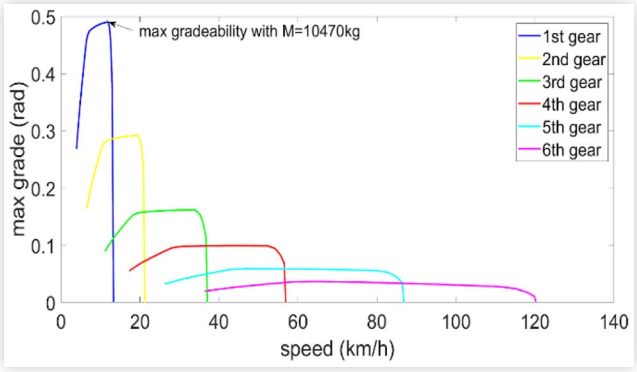

The values of speed and acceleration found with the methodology described above are compared with the declared values from the manufacturer in Table 6. The low errors in the estimation of the vehicle performance index prove the validity of the simulation approach and the reasonability of the assumptions reported in Table 5. However, a sensitivity analysis that was not reported here for brevity showed that increasing either the rolling coefficient up to 0.01 or the auxiliary power up to 10 kW only slightly affects the results of this analysis.The plots of maximum gradeability and acceleration, calculated using the actual vehicle mass, were also used to define the level of filtering for acceleration and to verify the elevation profile in Figure 1.

Fuel Consumption and Engine Efficiency

Figure 13 shows the estimated engine working points in trip #4 (no payload), colored according to the fuel flow rate obtained from the OBD. The full load torque is also reported.

Note that the values of mass flow rate included in the dataset do not correlate with the engine working point and cannot be used to estimate the engine efficiency. The same happens with exhaust temperature and flow rate. This can be explained by the typical lag in a turbocharged engine caused by the turbine-compressor inertia and the resulting delay between the control action on the fuel flow rate and the resulting variation of engine torque. Moreover, the acquired signals can be affected by a certain misalignment between OBD and PEMS data, as well as a certain level of noise. This could also explain why

TABLE 6 Validation of the model with ISUZU 6HK1-TCN.

Performance index	From vehicle datasheets [51]	Estimated	Relative error
Max speed (M=24000 kg)	118 km/h	119.8 km/h	+1.6%
Max Gradeability with M=24000 kg	22%	21.76%	-1%
Max Gradeability with M=15300 kg	35%	35.05%	0.14%

FIGURE 13 Full-load torque curve of the engine and operating points for trip #4 colored according to fuel flow rate.

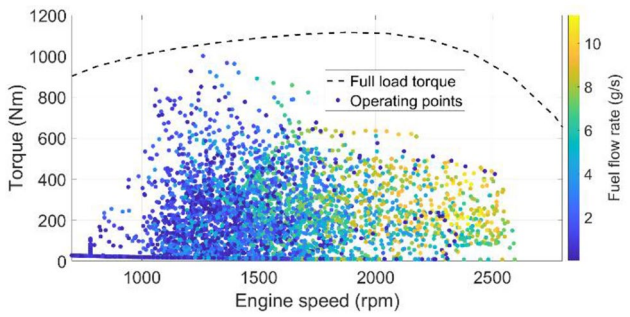

engine speed is not directly correlated to vehicle speed, as shown in Figure 14, where the measured values of engine rpm are plotted against the gear speed curves.

Development and Calibration of the Map-Based Model Since experimental data were not suitable to obtain a map of the engine fuel consumption or efficiency, the scaling procedure proposed in [52] was used. The map available in the MATLAB/Simulink powertrain library "Mapped CI Engine" was adopted as the reference engine. This library was particularly useful since it contains information on air mass flow, fuel flow, exhaust temperature, efficiency, and pollutant emissions. The maps are related to a 1.5L modern diesel engine with a minimum Brake Specific Fuel Consumption (BSFC) equal to 188g/kWh. These maps were used to adapt the maps of the general Simulink model (GM) to the ISUZU engine (IS). Using the well-known proportionality between torque and displacement (assuming the same mean effective pressure for both engines), it is possible to scale the torque as:

$$T_{IS} = T_{GM} \cdot \frac{V_{IS}}{V_{GM}} \tag{9}$$

Where V_{IS} and V_{GM} are the displacements of two engines. The speed of the engine is scaled according to the engine stroke S (assuming the same mean piston speed for both engines):

$$n_{IS} = n_{GM} \cdot \frac{S_{IS}}{S_{GM}} \tag{10}$$

FIGURE 14 Correlation between vehicle speed (from OBD or GPS) and engine rpm in the raw data.

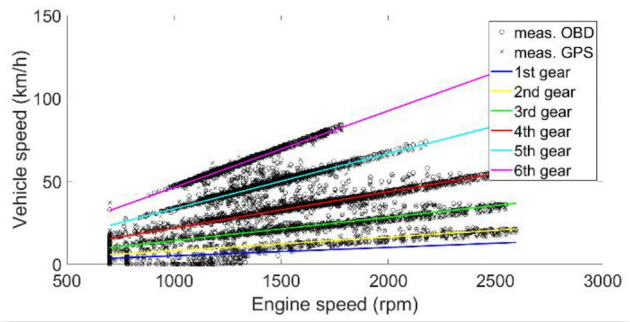

The mass flow rate of fuel was scaled as:

$$\dot{m}_{fS} = \dot{m}_{fGM} \cdot \frac{S_{IS}}{S_{GM}} \cdot \frac{V_{IS}}{V_{GM}} \tag{11}$$

A similar correction was applied to the mass flow rate of exhaust gases and pollutant emissions.

The efficiency map of the GM engine was divided by a correction factor to account for the older technology and degradation of the actual engine compared with the Simulink map, and for additional losses in the driveline (including clutch) that are not included in η_{gb}. A value of 1.49 for the correction factor was obtained by matching the experimental fuel consumption in trip #4. The engine maps obtained from the scaling procedure are shown in Figure 15.

Note that, as explained by Guzzella et al. [48], the validity of the map-based model is inadequate under very low-torque conditions. Therefore, at idle, the fuel and exhaust mass flow rates were obtained from the experimental data (0.5g/s and 0.035kg/s, respectively, as an average in all trips). Figure 16 compares the experimental and numerical values of fuel flow rate and cumulative fuel consumption along trip #4 after the fitting.

Validation of the Model The same correction factor, 1.49, was then applied to the fuel consumption map in all other trips without further turning. The plots in Figure 17 show a comparison of the experimental and numerical values of fuel flow rate and total fuel consumption. It can be noticed that for almost all cycles, the numerical values are within the ±5% error band of the experimental data. Even if no correction is applied for cold-start operation, the model captures fuel consumption very well, also in the case of mid and cold-start. The average error in terms of cumulative fuel consumption over the hot-start trips is 2.6%, as in the case of the cold- and mid-start trips. The limited values of MCTT are explained by the length of the trips.

The worst result is obtained for trip #22 (hot start). However, the trend of fuel flow rate is also well captured for this trip, as shown in Figure 18.

Cold-Start Correction for Fuel Consumption As in the analysis of the experimental data, to underline the effect of cold start, it would be necessary to limit the analysis to the first 400 seconds of the trips. However, in this part of the cycle, the mass flow rate is very low, below the accuracy of the proposed model. For this reason, the cold-start behavior is not simulated using the quasi-static approach; instead, it is analyzed in terms of additional fuel consumption and emissions based on the results in Table 4.

Emissions Regarding pollutant emissions, it is well known that the quasi-static approach is not suitable to predict them. To verify this, the stationary maps of NO_x and CO emissions available in the Simulink CI model were corrected to account for fuel consumption, as shown in Eq. (11). The numerical data for CO and NO_X were then

FIGURE 15 Maps of BSFC, exhaust temperature, fuel flow rate, and exhaust flow rate of ISUZU6HK1.

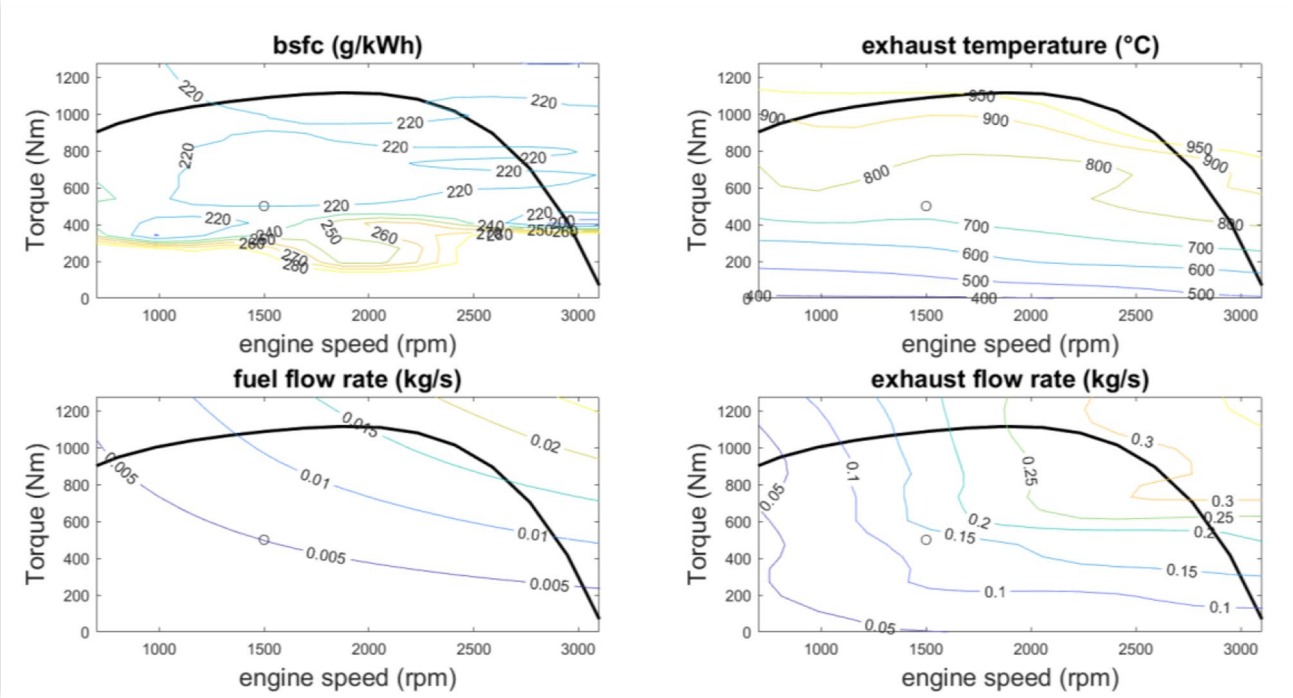

FIGURE 16 Calibration of the model on trip #4 in terms of fuel flow rate (top) and cumulative fuel consumption (bottom).

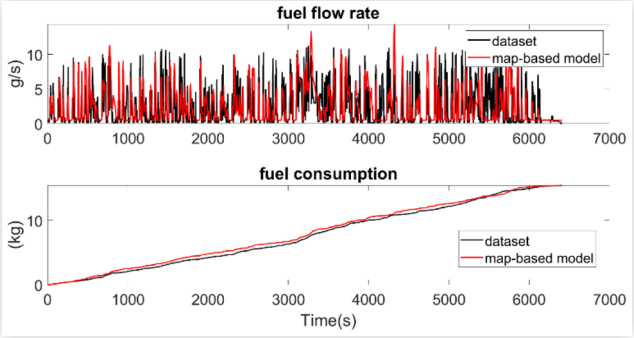

FIGURE 17 Validation of the map-based model for fuel consumption.

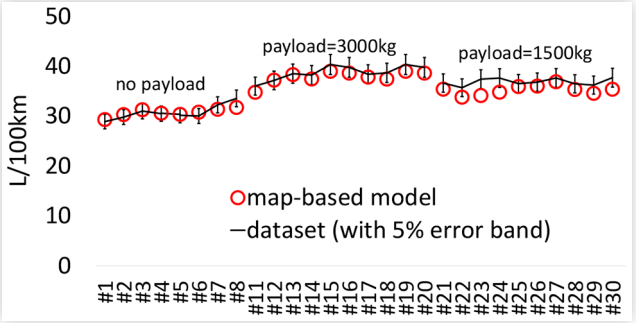

FIGURE 18 Validation of the model on trip #23 (worst-case) in terms of fuel flow rate (top) and cumulative fuel consumption (bottom).

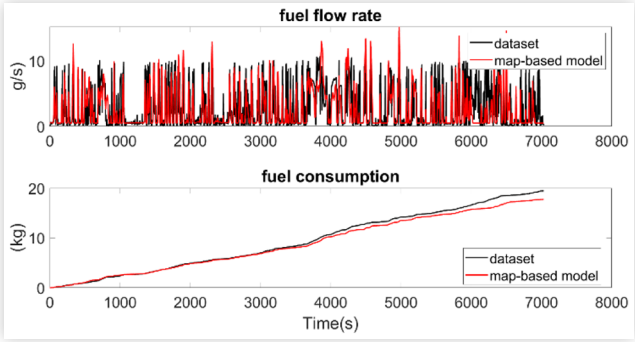

calibrated by matching the experimental data from trip #4 (Figure 19). Correction factors equal to 110 and 0.08 were found for CO and NO_x, respectively. As expected, the emissions calculated with these correction factors do not match the experimental data in the other trips, as shown in Figure 20 for trip #14.

Exhaust Mass Flow Rate and Temperature In terms of exhaust mass flow rate, the map of Figure 15 reports the exhaust temperature at the turbine exit (hot-end of the exhaust line) while the experimental data reports the values at the tailpipe exhaust where the PEMS system is positioned (cold-end). The losses of temperature in the exhaust line from the hot-end to the cold-end depend on

FIGURE 19 Calibration of the model by comparing experimental (PEMS) and numerical (map-based model) cumulative emissions on trip#4.

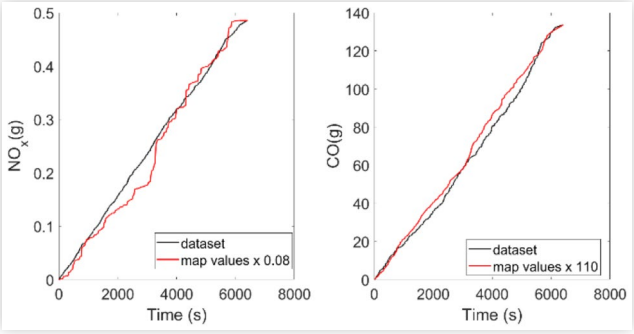

FIGURE 20 Application of the map-based model for emissions to trip #14.

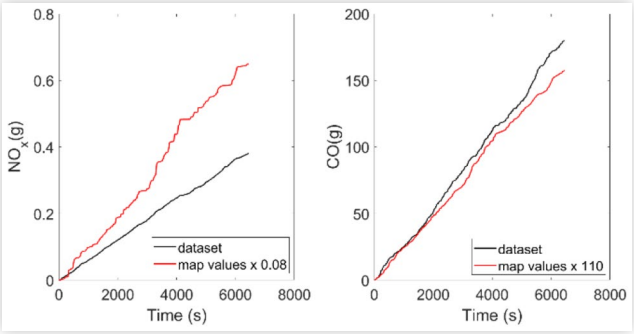

the engine operating point (as shown in Madaro et al. [53]). Since it was not possible to develop a detailed model in the present investigation due to a lack of details on the vehicle's exhaust line, a simplified procedure was considered. To obtain the exhaust temperature at the cold end (tailpipe), the temperature calculated at the hot end was reduced by 350°C, independently of the engine load and speed, and a moving window filter was applied. The value of 350°C was obtained by matching the experimental data for trip #4 and then applied to all other trips. An intermediate temperature was calculated as the average between the other two to study the WHR. The trends in mass flow rates are well captured for all trips, as shown in Figures 21 and 22 for trip #4 and trip #14, respectively. This is particularly true when the vehicle is not stopped or driven at very low speeds. When the engine is idling (as in trip #14 between 4200 and 4500s, for example), the modelled temperature decays faster than the experimental data, indicating the need to account for the thermal inertia in the exhaust line. Secondary causes of inaccuracies in the model may also be related to the differences in ambient temperatures and elevations between the first half and the second half of the trip (Figure 1).

Nevertheless, the results obtained with this simplified approach can be considered suitable for the goal of the projects, in particular for the sizing and modeling of the waste-heat recovery system. In fact, they capture

FIGURE 21 Validation of the proposed model in terms of exhaust flow rate (top), calibration of cold-end temperature, and estimation of intermediate temperature (bottom) on trip #4.

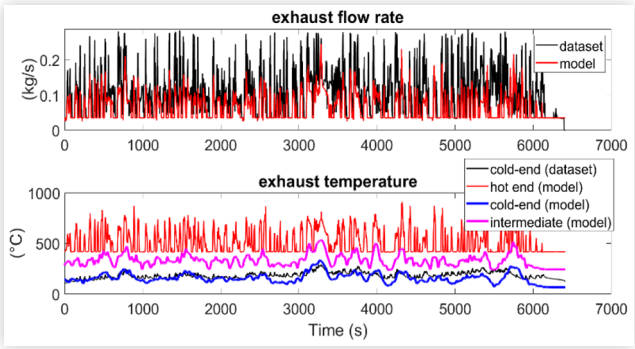

FIGURE 22 Validation of the proposed model in terms of exhaust flow rate (top), and estimation of hot-end, cold-end, and intermediate temperature (bottom) on trip #14.

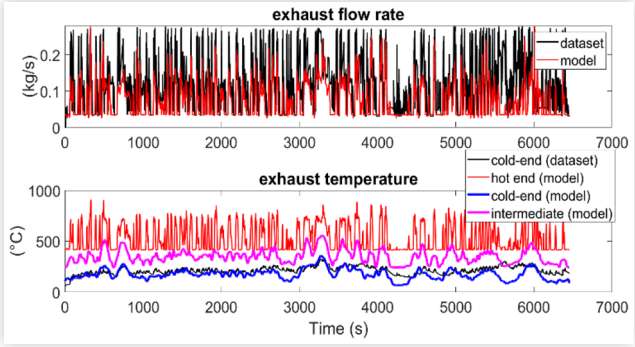

reasonably well the distribution plots of exhaust temperature (cold-end) and mass flow rate as shown in Figure 23. A data-driven approach based on Random Forest Regression (RFR) will be proposed in the continuation of the project for the prediction of exhaust temperature. Based on preliminary results, the RFR reduces the Root Mean Squared Error on temperature from 51.1 to 2.2°C and on mass flow rate to a third, compared with the methodology proposed here.

FIGURE 23 Distribution plots of exhaust temperature and mass flow rate in the dataset (left) and from the proposed model (right) for trip #4.

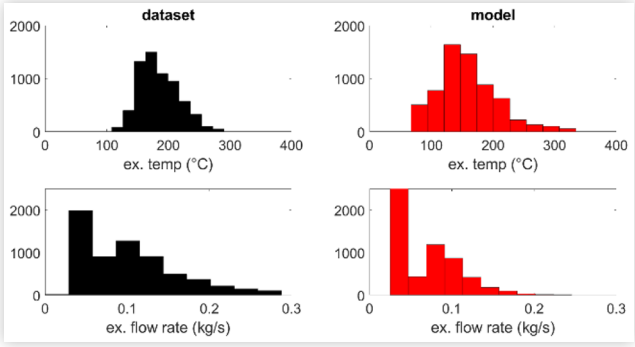

FIGURE 24 Correction to the map-based model for exhaust temperature at cold-start (trip #5).

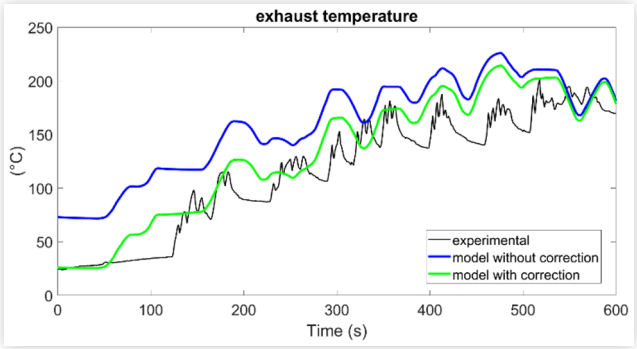

FIGURE 25 Correction to the map-based model for exhaust temperature at cold-start (trip #17).

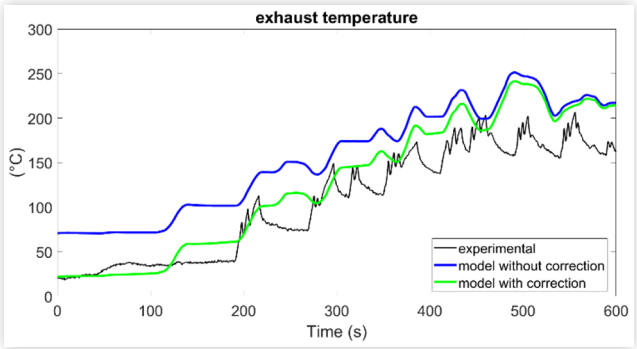

Cold-Start Correction for Exhaust Temperature An empirical correction for the cold-end exhaust temperature has been derived by using the experimental data at cold start reported in Figure 8:

$$\theta_{ext,c}(i) = \theta_{ext}\left(n_{ICE}(i), T_{ICE(i)}\right) - 50 \cdot \frac{\left(88 - \theta_{cool}(i)\right)}{68} \quad (12)$$

Where $\theta_{ext}(n_{ICE}(i), T_{ICE(i)})$ is the cold-end exhaust temperature calculated with the procedure described above, and $\theta_{cool}(i)$ is the coolant temperature at timestep (i). The application of this empirical equation to trips #5 and #17 is illustrated in Figures 24 and 25, respectively. The match with the experimental data is considered sufficient for the goals of the project. Similar results are obtained for the other cold-start trips.

Potentiality of Hybridization and WHR, and Future Activities

As explained previously, the ultimate goal of the IRIDESCENT project is to reduce fuel consumption and cold-start emissions by leveraging the synergy of exhaust WHR, hybridization, biodiesel fuel utilization, and phase-change thermal storage systems. The potential for heat recovery with an ORC has been analyzed in a previous paper [54], while hybridization is introduced here to exemplify the use of the proposed model within the project framework. A parallel hybrid electric architecture is considered, as shown in the simplified scheme of Figure 26.

The following hypotheses and simplifications are made for this preliminary analysis:

- The additional mass of the hybrid powertrain with or without ORC is negligible compared to the combined weight of the payload (3000 kg) and the truck.
- The engine is supposed to work at constant power when the vehicle is in traction and turned off at stops and braking.
- The engine speed at each time step is the same as in the original configuration (same gearbox and shift strategy).
- The analysis is performed with the original engine and with a downsized version, exploiting the scalability of the proposed model.
- The electric path manages the missing power between the required power and the engine contribution.
- The battery is sized according to the energy requirement of trip # 14, assuming a Depth of Discharge of 70%, a gravimetric energy density of 150 Wh/kg, and a C-rate of 15C in discharge.
- The regenerative braking power is limited to 7 kW to preserve battery health.
- A constant efficiency (η_{EM} = 0.9) is considered for the electric machine.
- The auxiliary power of 2 kW is assumed to be guaranteed by the battery or by the ORC [45] in the hybrid powertrain without or with WHR, respectively. This is a conservative hypothesis, as larger levels of electric power were found in the preliminary ORC analysis [54].
- Only hot-start operation is taken into account at this point.

FIGURE 26 Simplified scheme of the proposed architecture.

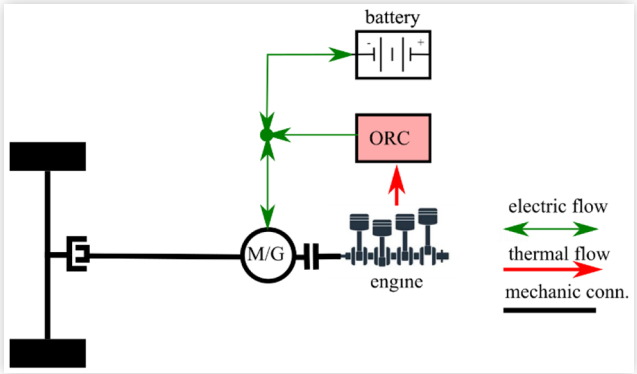

- The analysis is performed on trip #14 that belongs to the class of trips with a payload of 3000kg. Therefore, the additional mass of the powertrain does not affect the power request but reduces the payload.

At each time step, the power of the battery $P_{batt}(i)$ is calculated as:

$$P_{batt}(i) = P_{EM}(i) / \eta_{EM}^{\gamma} \quad (13)$$

Where the motor power is given by $P_{EM}(i) = P_w(i) - P_{ICE}(i)$.

In eq. (13), γ is equal to 1 or -1 when the electric machine operates as a motor or generator, respectively. The battery energy and the maximum battery power are used to size the battery by integrating $P_{batt}(i)$ according to the procedure described in [55]. A depth of discharge of 70% was assumed for the battery.

The engine power at time step "i" is calculated as:

$$P_{ICE}(i) = \begin{cases} 0 & if \ \ P_w(i) \le 0 \\ P_{ICE}d & if \ P_w(i) > 0 \end{cases} \quad (14)$$

Where the power setpoint $P_{ICE}d$ is a design variable that affects the size of the battery and the results of the hybrid electric configuration in terms of fuel consumption, exhaust temperature, and exhaust flow rate. A sensitivity analysis was performed in this investigation by increasing the value from 30 kW to 70 kW, and the results are shown in Figure 27. In particular, the top-left plot compares the total fuel consumption obtained with the conventional powertrain (dotted black line) with the consumption of the hybrid vehicle with the set-point varied from 30 to 70 kW (continuous red line). Fuel consumption for hybrid powertrain increases with $P_{ICE}d$, and from 58kW onward, the hybrid configuration consumes more fuel than the original one making the hybridization no more effective for fuel economy improvement.

On the other hand, increasing engine power $P_{ICE}d$ reduces the need for a larger battery (top right plot) and is advantageous in terms of exhaust enthalpy since both temperature and mass flow rate of exhaust gases increase (bottom plots of Figure 27). These last two results are due to the engine working points being moved towards the top-right part of the map where both temperature and mass flow rate are higher, which is the rationale of keeping constant the engine power. To show this effect, the constant power curves corresponding to $P_{ICE}d$ = {30,50,70} are superimposed to the engine maps of exhaust gas temperature and mass flow rate in Figure 28.

Based on the results in Figure 27, the value of 50 kW was chosen for $P_{ICE}d$ as a compromise between fuel consumption, battery mass, and average exhaust temperature. The detailed results of the simulation with $P_{ICE}d$ = 50 *kW*and the engine working points in the conventional and hybrid electric architecture with the two engines can be found in the Appendix.

Table 7 summarizes the results in terms of fuel consumption, battery size, exhaust temperature, and mass flow rate for the original configuration compared with the adoption of hybridization (with $P_{ICE}d$ = 50 kW) and WHR, together or separately. The exhaust temperature and mass flow rates are expressed in terms of average value and standard deviation in trip #14. The larger deviations of exhaust temperature and mass flow rates in the hybrid electric configurations are due to the choice of turning off the engine when the vehicle is at a standstill or braking.

For the hybrid electric configuration with ORC, a downsized 4-cylinder engine is also considered, while maintaining $P_{ICE}d$ = 50 kW. The results of Table 7 show that incorporating an Organic Rankine Cycle (ORC) system alone can reduce fuel consumption by approximately 3.5%, lowering it from 37.5 to 36.2 liters per 100 kilometers. However, this improvement comes with a trade-off: the available thermal power decreases because both the average temperature and the mass flow rate drop due to a lower average engine load. This highlights the need for a proper balance, as ORC systems can utilize waste heat efficiently, but their added weight and volume can negatively impact a vehicle's load capacity and overall efficiency. These physical constraints also serve as key indicators of the system's capital cost. To estimate the weight of an ORC system suitable for the application discussed in the paper, the authors reference a study by

FIGURE 27 Sensitivity analysis on the engine power $P_{ICE}d$ in the hybrid electric configuration without ORC and with the original engine.

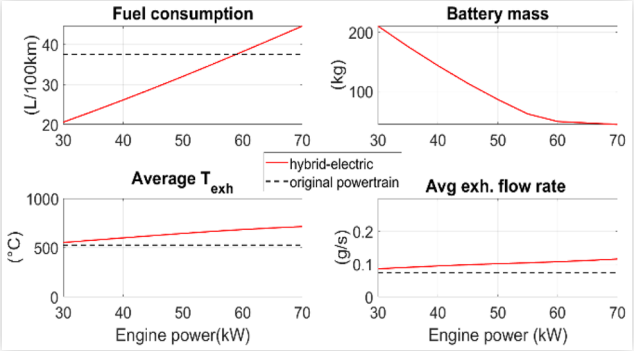

FIGURE 28 Superposition of constant power curves to engine maps of exhaust mass flow rate (left) and temperature (right)

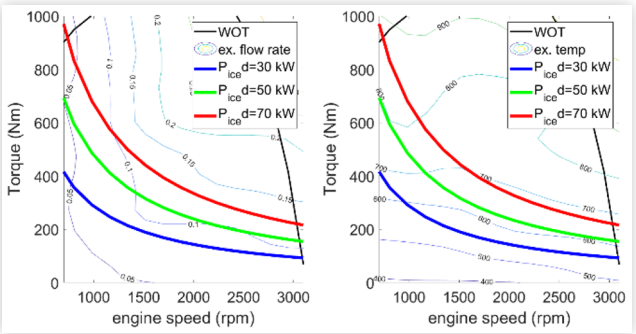

TABLE 7 Potentiality of hybridization and WHR calculated on trip #14 (payload 3000kg).

Configuration	Fuel consumption	Battery size	Exhaust temp (hot end): average value ± standard deviation	Exhaust mass flow rate: average value ± standard deviation
Unit	(L/100km)	(kWh)	(°C)	(g/s)
Original	37.5	-	525.7±128	0.0736±0.046
Original + ORC	36.2	-	502.0±143	0.0724±0.045
Hybrid electric	32.0	15.5	644.8±57	0.053±0.0527
Hybrid electric with ORC	32.0	12.9	644.8±57	0.053±0.0527
Hybrid electric with ORC and 4-cyl engine	31.8	12.9	725.3±57	0.043±0.041

Pili et al. [56], which evaluates several working fluids under typical exhaust gas conditions found in HDVs on highways. That study analyzes simplified ORC setups without recuperation, designed to be as lightweight as possible, and reports Power-To-Weight (PTW) ratios accordingly. Only the heat exchanger core weight is considered by Pili et al., because it is the component with the highest weight contribution [57]. Moreover, for a size between 2 and 4 kW, the projected weight is influenced primarily by the selected working fluid. For ORC systems operating with R245fa, the estimated weight ranges from approximately 17.3 kilograms for a 2 kW system to 34.9 kilograms for a 4 kW system. These results underscore the significant impact of the choice of fluid and system layout on overall weight, even at low power levels, which is a crucial consideration in mobile applications such as automotive waste heat recovery.

Hybridization without ORC and with the original engine reduces fuel consumption by 14.7% (from 37.5 to 32.0 L/100 km) and increases the average exhaust temperature by 22.7%. Exhaust temperature is also more stable, as proved by the reduction of its standard deviation. This result is due to the almost coincidental intersection of constant power and constant exhaust temperature curves in the engine map (Figure 15). Since the engine is turned off at stop and braking, however, the average mass flow rate decreases despite the almost constant exhaust flow rate of the engine when in traction. The addition of ORC does not affect the engine's working point but reduces the required battery mass by 16% (-17 kg). However, this is compensated for by the additional mass of the ORC. Note that the levels of fuel saving found in this work are strongly influenced by the simplifying hypotheses used in the sizing and management of the powertrain. These results require verification in the continuation of the paper. Nevertheless, they are of the same order of magnitude as found in similar studies [43].

The use of a downsized engine allows a further slight reduction of fuel consumption (31.8 L/100km) and an increase of 37.5% in the average temperature (thanks to the increased engine load) but a lower mass flow rate. Note that the last two configurations of Table 7 have the same engine operating power, but the full-load power is lower for the downsized engine.

An increase in temperature does not necessarily lead to a better exploitation of waste heat, as the temperature might be too high for the organic fluid or the phase change material (PCM). Moreover, the lower stability of the exhaust flow in the hybrid configuration (due to the engine being turned off). These aspects will be addressed in the continuation of the work, not only by proposing a realistic and optimized energy management strategy, but also by incorporating a PCM heat exchanger into the powertrain, as shown in Figure 26. Moreover, more accurate sizing and energy management will be performed for the entire powertrain, including hybridization, PCM, and WHR. The energy management will take into account the necessity of minimizing the MCTT to comply with emissions limits [58] and also to maximize the WHR. Within this scope, AI techniques will be considered to predict exhaust temperature at the mid-end, both with and without cold-start operation, thereby overcoming the limitations of the present analysis in terms of exhaust line simulation. Other issues to address in the continuation of the project are the role of aftertreatment devices in modern diesel engines and their requirements in terms of exhaust temperature and the backpressure caused by the heat exchanger.

Summary/Conclusions

The present investigation studies an experimental dataset acquired on the Isuzu 850 truck to quantify fuel consumption and exhaust enthalpy under real-world operating conditions, inclusive of different levels of payload and initial coolant temperature. The dataset is used to implement and validate a modeling approach combining engine maps with empirical correlation. The proposed model predicts very well not only the main vehicle performance indexes (max speed and gradability) but also the overall fuel consumption (and corresponding CO_2 emissions) with an average error of 2.6% over the 28 trips contained in the dataset. The effect of cold start was found difficult to model because of the low engine load in the first part of the vehicle. However, the expected additional consumption was estimated using experimental data.

In terms of exhaust enthalpy, the modeling approach, once tuned on one of the trips, gave reasonably accurate results on all other trips, proving the possibility of using such a model for the design and analysis of WHR systems like ORC and electrified powertrains.

The preliminary sizing and energy management of a hybrid electric configuration, which exploits the synergy between hybridization and WHR, resulted in a 15%

reduction in fuel consumption and a 37.5% increase in exhaust temperature. However, these results are affected by the strong simplifications made in this investigation. For this reason, the paper presents the future activities of the project planned to overcome the limitations of the analysis reported in this paper.

Another limitation of the present study is the use of a dataset related to a Euro 3 diesel engine. However, even if the values of exhaust temperature and mass flow rate could be different in a Euro 6 engine, the procedure proposed here is still valid since the dynamicity of the data would not be affected and the relative improvement in fuel consumption given by hybridization and ORC adoption should be the same as proved by comparison with similar works in literature.

References

1. Wang, X., Wang, C., Gao, T., Li, T. et al., "Analysis of the Engine Test Cycles from China VI heavy Duty Vehicle Standard and China Automotive Test Cycle," *E3S Web Conf.* 268 (2021): 01020, doi:10.1051/e3sconf/202126801020.
2. Barbosa, F.C., "Heavy Duty Diesel Emission Standards Regulation Evolution Review - Current Outcomes and Future Perspectives," SAE Technical Paper 2019-36-0174 (2020), https://doi.org/10.4271/2019-36-0174.
3. Clark, N.N. and McKain, D.L., "A Chassis Test Procedure to Mimic the Heavy-Duty Engine Transient Emissions Certification Test," *J. Air Waste Manag. Assoc.* (2001), doi:10.1080/10473289.2001.10464276.
4. Su, S. et al., "China VI Heavy-Duty Moving Average Window (MAW) Method: Quantitative Analysis of the Problem, Causes, and Impacts Based on the Real Driving Data," *Energy* 225 (2021): 120295, doi:10.1016/j.energy.2021.120295.
5. Andrych-Zalewska, M., "Analysis of Exhaust Emission Processes during the Real Driving Emissions Test," *Arch. Transp.* (2023), doi:10.5604/01.3001.0053.6085.
6. Varella, R.A., Giechaskiel, B., Sousa, L., and Duarte, G., "Comparison of Portable Emissions Measurement Systems (PEMS) with Laboratory Grade Equipment," *Appl. Sci.* 8, no. 9 (2018): 9, doi:10.3390/app8091633.
7. Merkisz, J., Lijewski, P., Fuć, P., Rymaniak, Ł. et al., "Measurement of Exhaust Emissions under Actual Operating Conditions with the Use of PEMS: Review of Selected Vehicles," 2017, doi:10.5772/INTECHOPEN.70442.
8. Ko, S.-U. et al., "NO_x Emissions from Euro 5 and Euro 6 Heavy-Duty Diesel Vehicles under Real Driving Conditions," *Energies* (2020), doi:10.3390/en13010218.
9. Hata, H. et al., "Real-World Measurement and Mechanical-Analysis-Based-Verification of NO_x and CO2 Emissions from In-Use Heavy-Duty Vehicle," *Atmospheric Measurement Techniques* 14, no. 3 (2020): 2115-2126, doi:10.5194/amt-2020-286.
10. Patil, S. et al., "Cold-Start WHTC and WHSC Testing Results on Multi-Cylinder Opposed-Piston Engine Demonstrating Low CO_2 Emissions while Meeting BS-VI Emissions and Enabling Aftertreatment Downsizing," *SAE Int. J. Adv. & Curr. Prac. in Mobility* 1, no. 1 (2019): 23-37, https://doi.org/10.4271/2019-26-0029.
11. Misra, C. et al., "In-Use NO_x Emissions from Model Year 2010 and 2011 Heavy-Duty Diesel Engines Equipped with Aftertreatment Devices," *Environ. Sci. Technol.* 47, no. 14 (2013): 7892-7898, doi:10.1021/es4006288.
12. Zavala, B. and Sharp, C., "Low Ambient Temperature Impact on a Low NO_X Demonstration System," *SAE Int. J. Adv. & Curr. Prac. in Mobility* 6, no. 1 (2023): 56-66, https://doi.org/10.4271/2023-01-0361.
13. Ximinis, J., Massaguer, A., and Massaguer, E., "NO_x Emissions below the Prospective EURO VII Limit on a Retrofitted Heavy-Duty Vehicle," *Appl. Sci.* 12, no. 3 (2022): 3, doi:10.3390/app12031189.
14. Sala, R., Krasowski, J., and Dzida, J., "The Influence of Engine Warm Up Phase on Nitrogen Oxides Emission for Heavy-Duty Euro VI Diesel Engine," 118 (2017), doi:10.1051/MATECCONF/201711800035.
15. Mendoza-Villafuerte, P. et al., "NO_x, NH3, N2O and PN Real Driving Emissions from a Euro VI heavy-duty vehicle. Impact of Regulatory On-Road Test Conditions on Emissions," *Sci. Total Environ.* 609 (2017): 546-555, doi:10.1016/j.scitotenv.2017.07.168.
16. Müller, V., Pieta, H., Schaub, J., Ehrly, M. et al., "On-Board Monitoring to Meet Upcoming EU-7 Emission Standards – Squaring the Circle between Effectiveness and Robust Realization," *Transp. Eng.* 10 (2022): 100138, doi:10.1016/j.treng.2022.100138.
17. Walter, E. and Walter, R., *Data Acquisition from Light-Duty Vehicles Using OBD and CAN* (SAE International, 2018)
18. Ge, Z. et al., "Real-Road NO_x and CO_2 Emissions of City and Highway China-6 Heavy-Duty Diesel Vehicles," *J. Environ. Sci.* 149 (2025): 330-341, doi:10.1016/j.jes.2023.11.018.
19. Sütheö, G. and Háry, A., "Comparison of Carbon-Dioxide Emissions of Diesel and LNG Heavy-Duty Trucks in Test Track Environment," *Clean Technol.* 6, no. 4 (2024): 4, doi:10.3390/cleantechnol6040070.
20. Girbés-Juan, V., Armesto, L., Hernández-Ferrándiz, D., Dols, J.F. et al., "Asynchronous Sensor Fusion of GPS, IMU and CAN-Based Odometry for Heavy-Duty Vehicles," *IEEE Trans. Veh. Technol.* 70, no. 9 (2021): 8617-8626, doi:10.1109/TVT.2021.3101515.
21. Gautam, M. et al., "Measurement of In-Use, On-Board Emissions from Heavy-Duty Diesel Vehicles: Mobile Emissions Measurement System," *SAE Trans.* 110 (2001): 2256-2269.
22. Abdelmegeed, M.A.E. and Rakha, H., "Heavy-Duty Diesel Truck Emissions Modeling," *Transp. Res. Rec.* 2627, no. 1 (2017): 26-35, doi:10.3141/2627-04.
23. Cao, Z. et al., "A Comprehensive OBD Data Analysis Framework: Identification and Factor Analysis of High-Emission Heavy-Duty Vehicles," *Environ. Pollut.* (2025): 125751, doi:10.1016/j.envpol.2025.125751.

24. Sütheő, G., Jagicza, M., and Baráth, B., "Emission Analysis of Liquefied Natural Gas and Diesel Heavy-Duty Trucks Using On-Board Monitoring Method," *J. Ecol. Eng.* 26, no. 2 (2025): 258-271, doi:10.12911/22998993/195574.
25. Dev, S. et al., "Highway Exhaust Emissions of a Natural Gas-Diesel Dual-Fuel Heavy-Duty Truck," SAE Technical Paper 2024-01-2120 (2024), https://doi.org/10.4271/2024-01-2120.
26. Rosero, F., Fonseca, N., López, J.-M., and Casanova, J., "Real-World Fuel Efficiency and Emissions from an Urban Diesel Bus Engine under Transient Operating Conditions," *Appl. Energy* 261 (2020): 114442, doi:10.1016/j.apenergy.2019.114442.
27. Zacharof, N. et al., "Estimating the CO_2 Emissions Reduction Potential of Various Technologies in European Trucks Using VECTO Simulator," SAE Technical Paper 2017-24-0018 (2017), https://doi.org/10.4271/2017-24-0018.
28. Schaberg, P., Harms, T., Schaberg, P., and Harms, T., "Development of Data-Driven Models for the Prediction of Fuel Effects on Diesel Engine Performance and Emissions," *SAE Int. J. Fuels Lubr.* 16, no. 3 (2023): 287-307, https://doi.org/10.4271/04-16-03-0020.
29. Keller, M., Neumann, M., Eichler, K., Pischinger, S. et al., "Model Predictive Control for an Organic Rankine Cycle System applied to a Heavy-Duty Diesel Engine," in *2020 IEEE Conference on Control Technology and Applications (CCTA)*, August 2020, 442-449, doi:10.1109/CCTA41146.2020.9206319.
30. Shahpouri, S., Gordon, D., Shahbakhti, M., and Koch, C.R., "Transient NO_x Emission Modeling of a Hydrogen-Diesel Engine Using Hybrid Machine Learning Methods," *Int. J. Engine Res.* 25, no. 12 (2024): 2249-2266, doi:10.1177/14680874241272898.
31. Meresht, N.B., Munshi, S., Shahbakhti, M., and McTaggart-Cowan, G., "Developing Machine Learning Models to Predict Methane and Nitrogen Oxide Engine-Out Emissions from a Heavy-Duty Natural-Gas Engine," in *Canadian Society for Mechanical Engineering (CSME) / Computational Fluid Dynamics Society of Canada (CFD Canada). International congress (2023: Université de Sherbrooke, Québec)*, Université de Sherbrooke. Département de Génie mécanique, 2023, accessed April 05, 2025, https://savoirs.usherbrooke.ca/handle/11143/21169.
32. Wang, X., Tsao, T.-C., Tai, C., Kang, H. et al., "Modeling of Compressed Air Hybrid Operation for a Heavy Duty Diesel Engine," *J. Eng. Gas Turbines Power* 131 (2009): 052802, doi:10.1115/1.3078788.
33. Neve, M., De Nicolao, G., Prodi, G., and Siviero, C., "Estimation of Engine Maps: A Regularized Basis-Function Networks Approach," *IEEE Trans. Control Syst. Technol.* 17, no. 3 (2009): 716-722, doi:10.1109/TCST.2008.2002040.
34. Liu, B., Ai, X., Liu, P., Zhang, C. et al., "Fuel Economy Improvement of a Heavy-Duty Powertrain by Using Hardware-in-Loop Simulation and Calibration," *Energies* 8 (2015), doi:10.3390/en8099878.
35. Williams, Z.L., Meruva, P., and Bitsis, D.C., "Machine Learning and Genetic Algorithm Method for Powertrain Development: Rapid Generation of Engine Calibration Maps," presented at the in *ASME 2022 ICE Forward Conference, American Society of Mechanical Engineers Digital Collection*, November 2022, doi:10.1115/ICEF2022-91169.
36. Pozzato, G., Rizzo, D., Onori, S., Pozzato, G. et al., "Sensitivity Analysis of a Mean-Value Exergy-Based Internal Combustion Engine Model," SAE Technical Paper 2022-01-0356 (2022), https://doi.org/10.4271/2022-01-0356.
37. Cozza, I.F. et al., "Application of a Machine Learning Approach for Selective Catalyst Reduction Catalyst 3D-CFD Modeling: Numerical Method Development and Experimental Validation," SAE Technical Paper 2023-24-0014 (2023), https://doi.org/10.4271/2023-24-0014.
38. Rizzoni, G., Guzzella, L., and Baumann, B.M., "Unified Modeling of Hybrid Electric Vehicle Drivetrains," *IEEEASME Trans. Mechatron.* 4, no. 3 (1999): 246-257, doi:10.1109/3516.789683.
39. Sorrentino, M., Mauramati, F., Arsie, I., Cricchio, A. et al., "Application of Willans Line Method for Internal Combustion Engines Scalability towards the Design and Optimization of Eco-Innovation Solutions," SAE Technical Paper 2015-24-2397 (2015), https://doi.org/10.4271/2015-24-2397.
40. Collins, K., Wartanian, R., Beer, F., and Hou, Y., "Moving Towards the Electrification of Medium- and Heavy-Duty Vehicles in the Inland Empire," *Mineta Transp. Inst.* (2024), doi:10.31979/mti.2024.2305.1.
41. Fioravanti, R., Sun, L., Mushet, R., Bolles, A. et al., "Impact of Medium- and Heavy-Duty Electric Vehicles and the Grid: An Address-Level/Bottom-Up California Case Study," *IEEE Power Energy Mag.* 22, no. 6 (2024): 76-82, doi:10.1109/MPE.2024.3456042.
42. Tuan, T.D., Phuoc, S.H., and Quang, T.N., "An Experimental Research to Evaluate the Effective of Regenerative Braking System Based on Actual Driving Conditions," in *2023 International Conference on System Science and Engineering (ICSSE)*, July 2023, 249-253, doi:10.1109/ICSSE58758.2023.10227190.
43. Villani, M., Lombardi, S., and Tribioli, L., "Performance Evaluation of a Heavy-Duty Diesel Truck Retrofitted with Waste Heat Recovery and Hybrid Electric Systems," *SAE Int. J. Electrified Veh.* 9, no. 1 (2020): 41-60.
44. Douadi, O., Ravi, R., Faqir, M., and Essadiqi, E., "A Conceptual Framework for Waste Heat Recovery from Compression Ignition Engines: Technologies, Working Fluids & Heat Exchangers," *Energy Convers. Manag. X* 16 (2022): 100309, doi:10.1016/j.ecmx.2022.100309.
45. Lombardi, S., Villani, M., Bella, G., and Tribioli, L., "Retrofit of a Heavy-Duty Diesel Truck: Comparison of Parallel and Series Hybrid Architectures with Waste Heat Recovery," SAE Technical Paper 2020-24-0015 (2020), https://doi.org/10.4271/2020-24-0015.
46. Joubert, J.W. and Gräbe, R.J., "Real Driving Emissions Data: Isuzu FTR850 AMT," *Data Brief* 41 (2022): 107975, doi:10.1016/j.dib.2022.107975.

47. "Isuzu Engines," Isuzu Diesel Engines, accessed March 19, 2025, https://www.isuzuengines.com/
48. Guzzella, L. and Sciarretta, A., *Vehicle Propulsion Systems: Introduction to Modeling and Optimization* (Berlin, Heidelberg: Springer, 2013), doi:10.1007/978-3-642-35913-2
49. Hammache, M., Michaelian, M., and Browand, F., "Aerodynamic Forces on Truck Models, Including Two Trucks in Tandem," 2001, accessed March 19, 2025, https://escholarship.org/content/qt6jr154q9/qt6jr154q9.pdf
50. Arts, G., "Analysis and Synthesis of Hybrid Truck Energy Management," PhD Thesis, TU Eindhoven Eindhoven, The Netherlands, 2007, accessed March 19, 2025, https://research.tue.nl/files/46975072/673408-1.pdf.
51. ISUZU, "F-SERIES FTR 850 ATM Specification Sheet," http://www.isuzu.co.za/, December 2017, https://iris.carsalesportal.co.za/cars-for-sale/brand/isuzu/F-SERIES-LIGHT-DELIVERY-IFS-CHASSIS-CAB/FTR850-amtspec-sheets-24334.pdf.
52. Sorrentino, M., Mauramati, F., Arsie, I., Cricchio, A. et al., "Application of Willans Line Method for Internal Combustion Engines Scalability towards the Design and Optimization of Eco-Innovation Solutions," SAE Technical Paper 2015-24-2397 (2015), https://doi.org/10.4271/2015-24-2397.
53. Madaro, F. et al., "Available Energy in Cars' Exhaust System for IoT Remote Exhaust Gas Sensor and Piezoelectric Harvesting," *Energies* 13, no. 16 (2020), doi:10.3390/en13164169.
54. Donateo, T., Cutuli, P., Vilotta, N., Algieri, A. et al., "Analysis of the Heat Content of Exhaust Gases from a Heavy-Duty Diesel Engine under Real-world Driving Conditions and Cold Start Operation," *J. Phys. Conf. Ser.* 2893, no. 1 (2024): 012103, doi:10.1088/1742-6596/2893/1/012103.
55. Donateo, T. and Chiodo, L.S., "Comparison of Lithium-Ion Battery Chemistries in the Hybridization of Ultralight Aircraft," SAE Technical Paper 2024-37-0017 (2024), https://doi.org/10.4271/2024-37-0017.
56. Pili, R., Castro Pastrana, J.D., Romagnoli, A., Spliethoff, H. et al., "Working Fluid Selection and Optimal Power-to-Weight Ratio for ORC in Long-Haul Trucks," *Energy Procedia* 129 (2017): 754-761, doi:10.1016/j.egypro.2017.09.116.
57. Lang, W., Colonna, P., and Almbauer, R., "Assessment of Waste Heat Recovery From a Heavy-Duty Truck Engine by Means of an ORC Turbogenerator," *J. Eng. Gas Turbines Power* 135, no. 042313 (2013), doi:10.1115/1.4023123.
58. Meier, F. and del Re, L., "Online Energy Management for Intermittent Operation of Hybrid Electric Vehicles at Low Temperatures," *IFAC-Pap.* 54, no. 20 (2021): 393-398, doi:10.1016/j.ifacol.2021.11.205.

Contact Information

Contact details for the main author should be included here. Details may include mailing address, email address, and/or telephone number (whichever is deemed appropriate).

Acknowledgments

We acknowledge financial support under the National Recovery and Resilience Plan (NRRP), Mission 4, Component 2, Investment 1.1, Call for tender No. 1409 published on 14.9.2022 by the Italian Ministry of University and Research (MUR), funded by the European Union – NextGenerationEU– Project Title IRIDESCENT – P2022YB8HY CUP F53D23009880001 - Grant Assignment Decree No. 5 adopted on 01/09/2023 by the Italian Ministry of University and Research (MUR).

Definitions/Abbreviations

BSFC - Brake Specific Fuel Consumption
CAN - Controller Area Network
CFD - Computational Fluid Dynamics
CO - Carbon Monoxide
CO_2 - Carbon Dioxide
DPF - Diesel Particulate Filter
DPFs - Diesel Particulate Filters
EGT - Exhaust Gas Temperature
FTP - Federal Test Procedure
GCM - Gross Combination Mass
GHG - Greenhouse Gas
GM - Generic Engine Model (Simulink Model)
GPS - Global Positioning System
GVM - Gross Vehicle Mass
HDV - Heavy-Duty Vehicle
HIL - Hardware-in-the-Loop
ICE - Internal Combustion Engine
MCTT - Matching Coolant Temperature Time
MUR - Ministry of University and Research
MVEM - Mean Value Engine Model
MVEMs - Mean Value Engine Models
NO_x - Nitrogen Oxides
OBD / OBD-II - On-Board Diagnostics (version II)
ORC - Organic Rankine Cycle
PCM - Phase-Change Material
PEMS - Portable Emissions Measurement Systems
PTW - Power-To-Weight
RDE - Real Driving Emissions
RPA - Relative Positive Acceleration
RPM - Revolutions Per Minute
SCR - Selective Catalytic Reduction
TES - Thermal Energy Storage
WHDC - World Harmonized Heavy-Duty Certification
WHR - Waste Heat Recovery

List of Symbols

A - Frontal area of the vehicle
A_{pos} - Positive acceleration
C_d - Aerodynamic drag coefficient

C_{rr} - Rolling resistance coefficient
d_s - Distance segment for RPA calculation
$\dot{m}_{fuel}$ - Fuel mass flow rate
$\dot{m}_{exh}$ - Exhaust mass flow rate
E_{bat} - Battery energy
γ - Electric machine mode (1 = motor, -1 = generator)
i_{gear} - Gear ratio
m - Vehicle mass
m_{eq} - Equivalent mass including inertial effects
n_{GM} - Engine speed of the generic Simulink model engine
n_{IS} - Scaled engine speed for the ISUZU engine
ω - Engine angular speed (rad/s or RPM)
P - Power (general)
P_{aux} - Auxiliary power consumption
P_{bat} - Battery power
P_{EM} - Electric motor/generator mechanical power
P_{eng} - Engine power
$P_{ICE}(i)$ - Engine power at time step i
P_{req} - Required power at wheels
$P_w(i)$ - Wheel power demand at time step i
r_w - Wheel radius
RPA - Relative Positive Acceleration
S_{GM} - Stroke length of the generic model engine
S_{IS} - Stroke length of the ISUZU engine
t_s - Time step (in RPA calculation)
T - Engine torque
$T_{e.WOT}$ - Wide-open throttle torque of the engine
T_{engine} - General engine torque
T_{GM} - Torque from the generic Simulink engine
T_{IS} - Scaled torque for the ISUZU engine
T_{FL} - Full load torque
v - Vehicle speed
ρ - Air density
η - Efficiency (gearbox or system)
η_{EM} - Electric machine efficiency
$\theta_{cool}(i)$ - Coolant temperature at time step i
$\theta_{ext}(n_{ICE}(i), T_{ICE(i)})$ - Cold-end exhaust temperature from model at engine speed and torque
$\theta_{ext,c}(i)$ - Corrected cold-end exhaust temperature at time step i
V_{GM} - Displacement of the generic model engine
V_{IS} - Displacement of the ISUZU engine

Appendix

The speed profiles of the regulatory cycles mentioned in the paper are shown in Figure 29.

The frequency distributions of the engine working point in the original and hybrid-electric configurations with the proposed simplified energy strategies are compared in Figure 30. The details of the power and energy flows in the hybrid configuration with ORC are reported in Figure 31 for the 6-cylinder engine.

FIGURE 29 Speed profiles of the regulatory driving cycle.

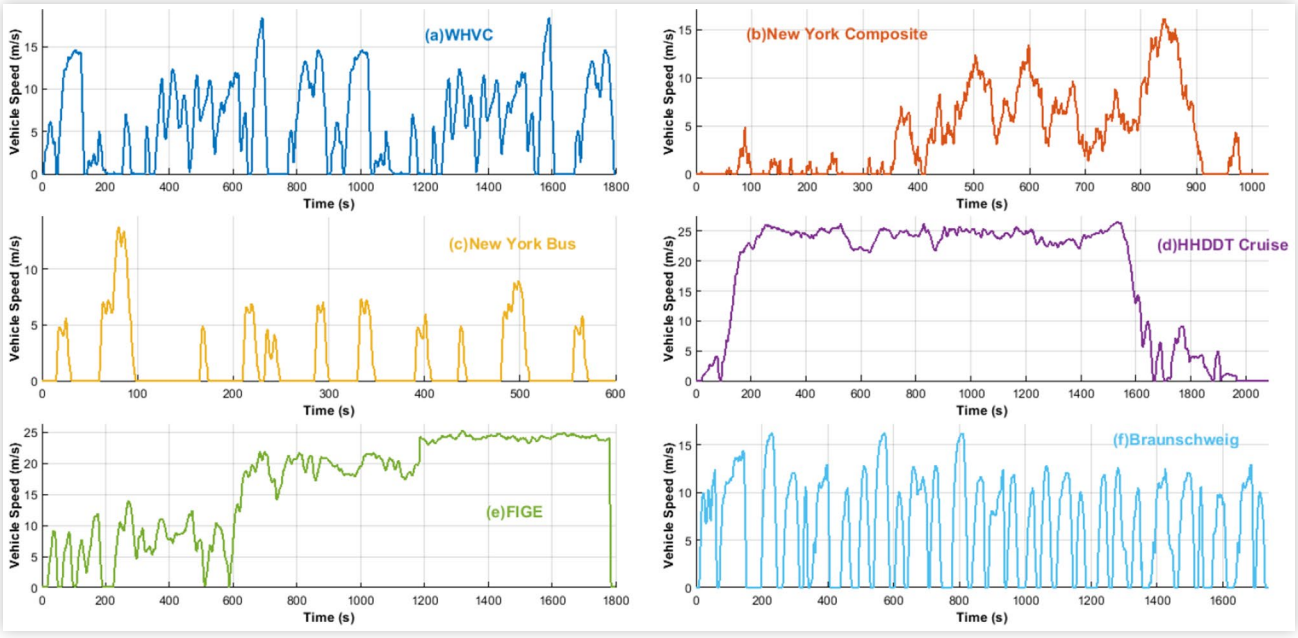

FIGURE 30 Frequency distribution of the engine working points (trip #14)

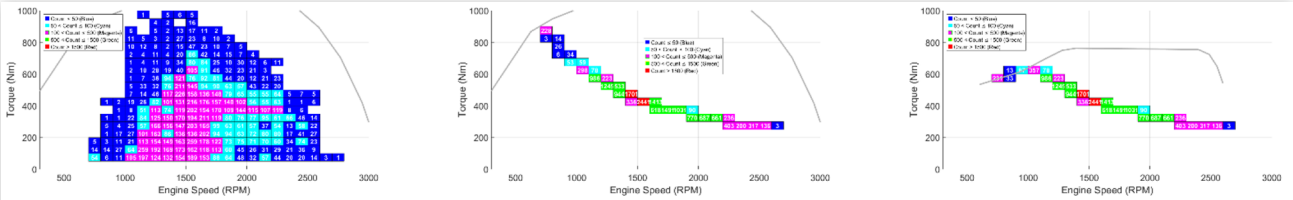

a) Original configuration

b) Hybrid electric configuration with the 6-cylinder engine

c) Hybrid electric configuration with the 4-cylinder engine

FIGURE 31 Results of the simulation of the hybrid electric configuration with ORC (trip #14, original 6-cylinder engine)

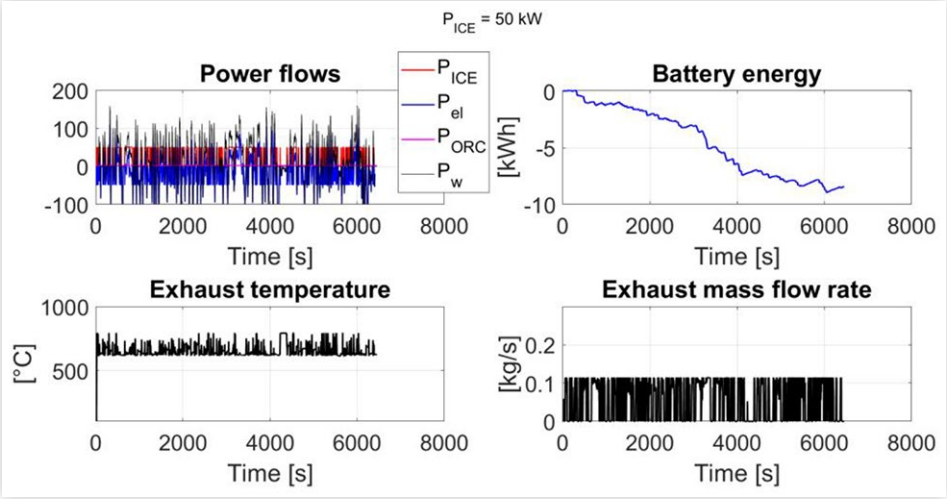

ISSN 0148-7191